HHS Public Access

Author manuscript

Acta Biomater. Author manuscript; available in PMC 2018 May 01.

Published in final edited form as:

Acta Biomater. 2017 May ; 54: 356–366. doi:10.1016/j.actbio.2017.02.043.

Micromechanical Anisotropy and Heterogeneity of the Meniscus Extracellular Matrix

Qing Li[1], **Feini Qu**[2,3], **Biao Han**[1], **Chao Wang**[1], **Hao Li**[4], **Robert L. Mauck**[2,3], and **Lin Han**[1,*]

[1]School of Biomedical Engineering, Science and Health Systems, Drexel University, Philadelphia, PA 19104, United States

[2]McKay Orthopaedic Research Laboratory, Department of Orthopaedic Surgery, Perelman School of Medicine, University of Pennsylvania, Philadelphia, PA 19104, United States

[3]Translational Musculoskeletal Research Center, Philadelphia Veterans Administration Medical Center, Philadelphia, PA 19104, United States

[4]College of Architecture and the Built Environment, Philadelphia University, Philadelphia, PA 19144, United States

Abstract

To understand how the complex biomechanical functions of the meniscus are endowed by the nanostructure of its extracellular matrix (ECM), we studied the anisotropy and heterogeneity in the micromechanical properties of the meniscus ECM. We used atomic force microscopy (AFM) to quantify the time-dependent mechanical properties of juvenile bovine meniscus at deformation length scales corresponding to the diameters of collagen fibrils. At this scale, anisotropy in the elastic modulus of the circumferential fibers, the major ECM structural unit, can be attributed to differences in fibril deformation modes: uncrimping when normal to the fiber axis, and laterally constrained compression when parallel to the fiber axis. Heterogeneity among different structural units is mainly associated with their variations in microscale fiber orientation, while heterogeneity across anatomical zones is due to alterations in collagen fibril diameter and alignment at the nanoscale. Unlike the elastic modulus, the time-dependent properties are more homogeneous and isotropic throughout the ECM. These results enable a detailed understanding of the meniscus structure-mechanics at the nanoscale, and can serve as a benchmark for understanding meniscus biomechanical function, documenting disease progression and designing tissue repair strategies.

Abstract

*Correspondence and requests for materials should be addressed to: Dr. Lin Han, Phone: (215)571-3821, Fax:(215)895-4983, lh535@drexel.edu.

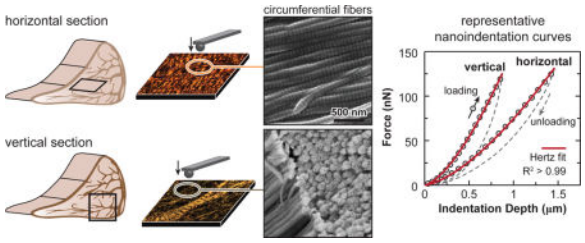

Keywords

meniscus; anisotropy; heterogeneity; extracellular matrix; nanoindentation

1. INTRODUCTION

The meniscus is an essential component of the knee joint, responsible for stability, load transmission and lubrication [1]. To enable efficient transmission of the complex tensile, compressive, and shear stresses, the extracellular matrix (ECM) of meniscus possesses a unique, hierarchically structured framework that is both heterogeneous and anisotropic at multiple length scales [2]. At the macroscale, the outer and middle zones mainly sustain circumferential tensile “hoop” stresses to provide joint stability [3]. In this region, the ECM is dominated by circumferentially aligned type I collagen fiber bundles. By contrast, the inner zone of the meniscus is mostly under compressive loads [4] to reduce cartilage loading [5], and the ECM has less aligned collagen fibers as well as a higher concentration of proteoglycans [6, 7]. At the microscale, the circumferential fibers are encapsulated by a ~ 100–200 μm thick superficial lamellar layer [2] composed of radially oriented fibers. These fibers emanate into the meniscus interior as “radial tie fibers”, and interdigitate throughout the circumferential fibers [8–10]. In between fibers, there exist proteoglycan-rich micro-domains that play a role in local strain transfer and regulate cell mechanotransduction [11]. On top of the superficial lamellar layer, there is a ~ 10 μm thick surface layer of transversely aligned fibrils, a feature similar to the surface of articular cartilage, its loading counterpart [12]. At the nanoscale, adjacent collagen fibers share several individual collagen fibrils, and are interconnected by these fibrils spanning across them (Fig. 1a). This hierarchical, intertwined structure enables the meniscus to sustain a complex array of tensile, compressive and shear loads, and to retain its load bearing capability even in the case of a radial tear that spans 50% across the tissue width [13].

Meniscal damage is a common cause of joint injury [1], which can lead to the development of post-traumatic osteoarthritis (PTOA) [14], a prevalent form of osteoarthritis (OA) among the younger population [15]. Unfortunately, similar to articular cartilage, the meniscus has limited self-healing capabilities, especially in the avascular, proteoglycan-rich inner zone [16]. To repair damaged meniscus and recover normal joint function, it is necessary not only to replicate the whole tissue morphology of the native meniscus [17], but also to restore its matrix structural heterogeneity at the nano-to-microscale [18], which is critical for the tissue to perform its specialized tissue-level properties [1]. To this end, it is imperative to understand the structure-mechanical function principles of the native meniscus ECM at multiple length scales [19]. However, current mechanical knowledge of the meniscus is

mostly limited to the tissue-level, and it is unclear how such complex ECM structure is connected with its mechanical properties [20]. Recently, a few studies started to investigate meniscus mechanics at nm- to-μm scales via instrumented nanoindentation [21, 22] and atomic force microscopy (AFM)-nanoindentation [23–25]. These studies demonstrated the potential of nanomechanical tests in revealing the small scale mechanical characteristics of the meniscus. However, these studies did not intend to focus on the anisotropy or heterogeneity associated with its ECM nanostructure. Without such knowledge, it is challenging to connect the meniscus disease etiology and pathogenesis with its structural complexity [26], or to design biomaterials that can replicate the functions of native tissue [27].

The objective of this study was to quantify the anisotropic and heterogeneous micro mechanics of the meniscus ECM. Inspired by the first, seminal AFM-nanoindentation work on the meniscus [23], we harvested menisci from calf knees, and cryotomed these tissues into micro-sections to expose different structural units of the ECM interior. AFM-based nanoindentation and ramp-and-hold force relaxation were applied to quantify the effective indentation modulus, and time-dependent mechanical properties of different ECM regions. The AFM tests resulted in deformation on the order of 1 μm, reflecting the properties of collagen fibrils at the nano-to-microscale, rather than fibers or fascicles at larger length scales. To connect the biomechanical outcomes with the ECM nanostructure, we analyzed collagen fibril structure at the nanoscale. These results provided new insights into native meniscus ECM biomechanics at multiple scales, further enriching our knowledge of tissue structure-function relationships [28].

2. METHODS

2.1 Sample preparation

Menisci were dissected from juvenile (≤ 3 months old) cows ($n = 3$) [29]. Multiple animals were used to confirm that the observed micromechanical anisotropy and heterogeneity features were consistent within the population. The outer, middle, and inner zones of the meniscus central body were isolated and embedded in Optimal Cutting Temperature (OCT) media. Each zone was cryo-sectioned transversely and radially onto glass slides to produce ≈ 20 μm thick horizontal and vertical sections, respectively (Fig. 1b). For horizontal sections, samples containing the intact surface, superficial (~ 100 μm from the surface on the tibial side) and deep zones (> 500 μm into the tissue) were taken parallel to the tibial surface. For vertical sections, samples from the central region were taken. Following standard the cryopreservation procedure [23, 24], samples were stored at −20°C in OCT for less than one week until AFM-nanoindentation tests.

2.2 AFM-nanoindentation and ramp-and-hold force relaxation

Prior to testing, sections were thawed and washed in phosphate buffered saline (PBS). On each section, AFM-nanoindentation was performed using microspherical colloidal tips ($R \approx 5$ μm, nominal $k \approx 0.6$ N/m, HQ:NSC36/Tipless/Cr-Au, cantilever C, NanoAndMore, Watsonville, CA) and a Dimension Icon AFM (BrukerNano, Santa Barbara, CA) at 10 μm/s indentation rate up to a maximum load of ≈ 120 nN (Fig. 1c). For each microstructural

region of each section (Fig. 1b,c), indentation was performed on at least 10–15 different locations. For each structural unit, the relationship between the indentation orientation and the collagen fiber axis was summarized in Table 1. At the same location, nanoindentation was repeated three times, where the high repeatability of indentation curves suggested negligible irreversible plastic deformation. During all indentation measurements, tissues were immersed in PBS (0.15 M, pH = 7.4) with protease inhibitors (Pierce) to minimize post-mortem degradation and to maintain physiological-like fluid environment.

To study the time-dependent micromechanics of the meniscus, a ramp-and-hold force relaxation test was performed via AFM. Immediately following the indentation, the *z*-piezo was held at a constant position for ≈ 30 seconds, resulting in an approximately constant indentation depth. During this period, both the *z*-piezo displacement and cantilever bending were recorded as a function of time at 500 Hz sampling rate, from which, the temporal profiles of indentation force, $F(t)$, and depth, $D(t)$ (mostly constant), were extracted.

2.3 Micromechanical data analysis

At each indentation location, indentation force versus depth (*F–D*) curve was obtained by calibrating the cantilever deflection sensitivity on a mica substrate and spring constant via thermal oscillation [30]. The effective indentation modulus (E_{ind}) was calculated by fitting the whole loading portion of each *F-D* curve to the finite thickness-corrected Hertz model [31] via least squares linear regression (Fig. 1c):

$$F=\frac{4}{3}\frac{E_{\mathrm{ind}}}{(1-v^2)}R^{1/2}D^{3/2}C_{\chi}(F,D,H,R) \quad (1)$$

where ν is the Poisson's ratio (≈ 0 for bovine meniscus [32]), R is the tip radius, H is the section thickness, and C_{χ} is the substrate constraint correction factor that depends on *F, D, H* and *R*. Here, E_{ind} represents the effective resistance to indentation at a finite indentation rate ≈ 10 μm/s, instead of the instantaneous modulus.

For each ramp-and-hold relaxation test, the relaxation segment of indentation force, $F(t)$, was fitted to a five-element spring-dashpot model to extract two time constants, τ_1 and τ_2 ($\tau_1 < \tau_2$),

$$F(t)/C_{\chi}=B_0+B_1\exp(-t/\tau_1)+B_2\exp(-t/\tau_2) \quad (2)$$

where the correction factor C_{χ} was applied to account for the substrate effect due to finite specimen thickness. Then, the fitting parameters of B_0, B_1 and B_2 were used to calculate the time-dependent material properties within the Hertzian deformation framework. Following the analysis procedure established by Mattice et al. [33] for relaxation following indentation at a finite ramp rate, we extracted the temporal indentation modulus, $E(t)$,

$$E(t)=E_{\infty}+E_1\exp(-t/\tau_1)+E_2\exp(-t/\tau_2), \quad (3)$$

where,

$$E_{\infty}=\frac{B_0(1-v^2)}{D_{max}^{3/2}(4\sqrt{R}/3)} \quad (4)$$

and

$$E_k=\frac{B_k(1-v^2)}{(RCF_k)D_{\max}^{3/2}(4\sqrt{R}/3)}, k=1,2. \quad (5)$$

Here, E_∞ is the equilibrium indentation modulus, E_1 and E_2 are the time-dependent moduli corresponding to the short and long term relaxation mode, respectively. The factor RCF_k, is the "ramp correction factor" that accounts for the finite indentation ramp rate [33, 34],

$$RCF_k=\frac{\tau_k}{t_R}[\exp(t_R/\tau_k)-1], k=1,2. \quad (6)$$

where t_R is the total rise time of the indentation ramp segment. As a result, this model yielded the equilibrium modulus, E_∞, and the time-dependent properties corresponding to the two relaxation modes, (E_1, τ_1) and (E_2, τ_2). The instantaneous indentation modulus, E_0, was estimated as,

$$E_0=E_\infty+E_1+E_2. \quad (7)$$

We therefore used the ratio of equilibrium versus instantaneous modulus, E_∞/E_0, as an indicator of the degree of elasticity. This method has been used to reveal the time-dependent mechanical properties of costal cartilage [35], the insertional zone of meniscal attachments [36], as well as poly(ethylene glycol) (PEG)-based hydrogels [37]. In this study, the implement of RCF_k resulted in minor changes to E_1 and E_2 (e.g., RCF_1 = 1.30 ± 0.06, RCF_2 = 1.00 ± 0.01, mean ± 95% CI, for the outer zone horizontal section of circumferential fibers), and did not affect the observed trends or conclusions.

2.4 Collagen nanostructure analysis

Since the fiber-level microstructure of the meniscus ECM has been revealed in detail by optical microscopy [9, 10], this study focused on the fibril-level, nanoscale structure of collagen. Immediately after AFM tests, each section was fixed with Karnovsky's fixative (Electron Microscopy Sciences, Hatfield, PA), dehydrated in a series of graded water-ethanol and ethanol-hexamethyldisilazane (HMDS) mixtures [38], and dried in air to retain the 3D collagen architecture. Scanning electron micrographs (SEM, Zeiss Supra 50VP) were acquired on samples coated with ~ 6 nm thick platinum. In addition, tapping mode AFM images were taken in ambient conditions on uncoated samples using nanosized silicon tips ($R \approx 10$ nm, $k \approx 42$ N/m, NCHV, BrukerNano) and the Dimension Icon AFM (BrukerNano).

For histology, separate deep zone sections were stained with Alcian Blue and Picrosirius Red (PSR) and imaged under polarized light to visualize proteoglycans and collagen fiber bundle organization at the microscale.

For each animal, five SEM images were taken from a 5 μm × 5 μm region of interest (ROI) within each structural unit. The collagen fibril diameter, d_{col} (in nm), and fibril alignment orientation angle, θ (in rad), were measured from each image by two blinded observers via ImageJ (≈ 100 fibrils per image). To compare fibril diameter among different structural units, values of d_{col} were pooled from multiple images of the same unit from all three animals. To compare the degree of collagen fibril alignment, we first offset values of θ by their average angle, μ_θ, to ensure $\mu_\theta = 0$ within each ROI. Next, we pooled all values from different ROIs of the same structural unit. In addition, since fibril orientation angles are axial data without directions (i.e., θ and $\theta + \pi$ are equivalent), we converted the values of 0 to occupy the whole circular space of $[-\pi\ \pi]$ by multiplying θ by a factor of two [39]. We then fitted the distribution of θ for each structural unit with the von Mises probability density function, which is the analog of normal distribution in the circular space,

$$f(\theta;\mu_\theta,\kappa)=\frac{1}{2\pi I_0(\kappa)}\exp[\kappa\cos(\theta-\mu_\theta)] \quad (8)$$

where κ is the concentration parameter (analogous to the inverse of variance), and $I_0(\kappa)$ is the zeroth order modified Bessel function of the first kind. Here, κ is a measure of how closely the vectors of θ cluster around the average angle μ_θ, and a greater value of κ indicates a higher degree of fibril alignment.

2.5 Statistical analysis

To avoid the assumption of normal distribution of the data, we used nonparametric statistical tests on the micromechanical properties, including E_{ind}, E_∞, E_1, E_2, E_∞/E_0, τ_1, and τ_2. The Mann-Whitney U test was used to examine the impact of indentation orientation on the same structural unit. The Kruskal-Wallis test followed by the Tukey-Kramer multiple comparison was used to examine the differences among various structural units and anatomical regions, and to examine the zonal variation of each structural unit. For each mechanical parameter, data was pooled from the three animals, as we did not find statistically significant differences between individual animals (e.g., Fig. 2a). For structural data, since ≥ 300 fibrils were measured for each structural unit, according to the central limit theorem, the parametric unpaired two-sample *t*-test was used to compare d_{col} of inner versus outer zones for each structural unit, and one-way ANOVA followed by the Tukey-Kramer multiple comparison was used to compare different structural units within each of the inner and outer zone. For fibril orientation data, θ, the Mardia and Jupp test of concentration equality [40] was applied to compare the von Mises concentration parameter κ between inner and outer zones for each structural unit, and to compare κ across structural units within the same zone with the Bonferroni family-wise error correction. In all the tests, a *p*-value of less than 0.05 was taken as statistically significant.

3. RESULTS

We detected salient anisotropy in the micromechanical properties of the circumferential fibers, the major structural component of the meniscus ECM (Fig. 2). For all animals, indentation on the vertical section (E_{ind} = 179 ± 22 kPa, mean ± 95% CI) yielded higher moduli than that on the horizontal section (E_{ind} = 58.4 ± 5.8 kPa). This trend was the same whether testing individual animals or examining the pooled data from all three animals (Fig. 2a). For time-dependent properties, following the trend of E_{ind}, the horizontal section also yielded lower equilibrium modulus, E_∞ as well as moduli corresponding to the short term (E_1) and long term (E_2) relaxation, while the degree of elasticity (E_∞/E_0) was similar on both sections (Fig. 2b). The five-element relaxation model fit showed that short term relaxation was a more dominant mode than the long term one for both sections ($E_1 > E_2$). Meanwhile, for the short term relaxation, both sections had similar τ_1, while for the long term relaxation, the horizontal section showed moderately longer τ_2 (Fig. 2b). On both sections, the alignment and structure of the circumferential fibers were revealed by histology at the microscale and SEM at the nanoscale (Fig. 2c).

We detected significant variations of E_{ind} amongst various ECM structural units, as shown for the outer zone (Fig. 3). On the vertical section, the circumferential fibers exhibited higher E_{ind} than other units, while on the horizontal section, a similar E_{ind} was found across all three units. The intact surface, on the other hand, had the lowest E_{ind} In addition, heterogeneity of E_{ind} was also observed between the tension-bearing outer and middle zones versus the compression-bearing inner zone (Fig. 4). For the circumferential fibers, on the vertical section, E_{ind} of the outer zone was 3.2 ± 0.8 times (mean ± 95% CI) higher than that of the inner zone. On the horizontal section, such difference was much reduced (1.6 ± 0.4 times, Fig. 4a). As a result, the degree of anisotropy was substantially lower in the inner zone, where the ratio of E_{ind} between vertical versus horizontal section was 2.1 ± 0.7 times in the inner zone, and 3.3 ± 0.7 times in the outer zone (Fig. 4a). Interestingly, unlike the circumferential fibers, the other units, including surface, superficial layer and radial tie fibers, did not exhibit significant zonal variations (Fig. 4b). In addition, since the middle zone had similar E_{ind} as the outer zone, this study primarily focused on differences between the inner and outer zones.

In contrast to the salient heterogeneity in E_{ind}, the time-dependent mechanical characteristics were more homogeneous (Fig. 5). The modulus values, including E_∞, E_1 and E_2, followed similar trends as E_{ind} (data are not shown for E_1 and E_2). However, the degree of elasticity (E_∞/E_0) and the relaxation time constants (τ_1 and τ_2) were relatively consistent amongst different structural units (Fig. 5a) and across different zones (Fig. 5b) despite variations in matrix composition and collagen fibril structure. For the circumferential fibers, vertical sections yielded moderately shorter τ_2 only in the outer zone, but had similar τ_1 in comparison to the horizontal section in both outer and inner zones (Figs. 2b, 5b). However, one exception to this finding occurred on the surface, which had similar time constants, but lower E_∞/E_0 and E_∞ compared to all other interior structural units (Fig. 5a).

The ECM collagen fibril nanostructure was revealed by SEM and AFM (Fig. 6a,b). Consistent with previous reports on human [2] and bovine [41] menisci, collagen fibrils on

the meniscal surface were oriented randomly within the transverse plane. In the interior, the fibrils were aligned along the fiber axis within each structural unit: circumferentially for circumferential fibers, and radially for superficial layer and radial tie fibers. Quantitative analysis showed that random fibrils on the surface were significantly thinner compared to other regions ($p < 0.0001$). For all structural units, fibrils in the outer zone are thicker than those in the inner zone (Fig. 7a). In addition, circular analysis using the von Mises model (e.g., Fig. 6c) confirmed the relative randomness of collagen fibril orientation on the surface ($\kappa < 0.5$), and high degree of alignment in the interior units (Fig. 7b). In the superficial layer, similar κ was detected between the two regions. In both the radial tie fibers and circumferential fibers, the concentration was higher in the outer zone. Furthermore, in the inner zone, similar κ were observed among the three interior units; in the outer zone, they were significantly different, where radial tie fibers had the highest κ, while superficial layer had the lowest.

4. DISCUSSION

4.1 Anisotropy of the circumferential fibers

The micromechanical anisotropy of circumferential fibers (Fig. 2) is not intuitive. For fibrous tissues, indentation normal to the fiber axis would create long range tensile stress within the fiber plane [42], while indentation parallel to the fiber axis results in fibril compression, bending or buckling [43]. On vertical sections, where indentation was performed parallel to the fiber axis, the measured E_{ind} was higher than that on horizontal sections, where indentation was performed normal to the fiber axis. This observation seems contradictory to the fact that meniscus is stiffer in tension than in compression [44]. However, this finding can be explained by the hierarchical structure of the meniscus ECM collagen fibers and the fact that deformation takes place locally, i.e., at the microscale. In the ECM, collagen undulation and crimping are present at both the fibril level (nm-scale, black arrows, Fig. 2c) and the fiber level (μm-scale, white arrowheads, Fig. 2c). In accordance, the tensile response of meniscus is highly nonlinear [44]: at small strains ($\varepsilon << 5\%$), the stiffness is very low, corresponding to the “toe region” of the stress-strain curve; once the strain reaches a critical uncrimping level (≈ 5–10% [45]), i.e., point at which collagen fibers are fully uncrimped, the stiffness increases drastically, corresponding to the “linear region”. Here, the deformation scale (~ 1 μm) is at least one order lower than the fiber crimping periodicity (~ 30 μm), and similar to the fibril crimping periodicity (~ 1 μm, Fig. 2c). Local strain induced by nanoindentation therefore does not exceed the critical uncrimping level. As a result, fibril uncrimping and sliding, instead of tensile stretching, dominate the indentation response [46, 47]. In fact, on the horizontal section, E_{ind} is $> 10^3 \times$ lower than macroscopic linear region tensile moduli of meniscus circumferential fibers (~ 100 MPa) [3], but is consistent with previous nanoindentation results on porcine [23] and human [24] menisci at similar deformation scales. On the other hand, within each fiber, the fibrils are highly aligned and densely packed (Fig. 2c). Due to lateral constraint from interfibrillar contact and fiber bundling, indentation parallel to the fiber axis can result in a continuous multiaxial stress field, leading to an indentation response similar to a material continuum, which is much less compliant than bending or buckling of discrete fibrils [48]. These effects together contribute to the observed anisotropy (Fig. 2a).

It should be noted that the modulus contrast reported here (Fig. 2) does not accurately reflect the intrinsic material anisotropy. Under nanoindentation, the indenter tip introduces a multiaxial stress and strain field, and the modulus estimated by the isotropic Hertz model is an effective measure of the compression resistance governed by the constitutive response of material properties at all axes [49]. As shown for mineralized biological tissues of bone [50] and ganoine [51], such multiaxial loading profile can obscure the intrinsic anisotropy. A more accurate assessment of anisotropy has been achieved by analyzing the shape of indentation residual via an anisotropic mechanics model [50], or by uniaxial compression on focused ion beam-machined micro pillars [52]. For soft tissues such as the meniscus, however, its hydrated nature prevents the use of the residual shape analysis or uniaxial microcompression. A more accurate measure of its intrinsic anisotropy would rely on indenting surfaces prepared by sectioning multiple orientations in combination with anisotropic mechanics models [53].

4.2 Heterogeneity across structural units

The heterogeneity of indentation modulus E_{ind} among different structural units, as shown for the tension-bearing outer zone (Fig. 3), can be attributed to the complexity of ECM collagen fiber structure. The superficial layer and radial tie fibers are both composed of radially aligned fibers with nano-to-microscale crimping. On the vertical section, when indentation is normal to their fiber axes, they undergo fiber uncrimping and sliding, yielding lower E_{ind} than circumferential fibers (Fig. 3). On the horizontal section, when indentation is normal to the fiber axes of the circumferential fibers and superficial layer, both units undergo uncrimping and sliding, yielding similar E_{ind}. For radial tie fibers, the fiber axes bifurcate randomly within the radial plane [10], and horizontal slices thus expose oblique fiber cross-sections, leading to a mixed response of fibril uncrimping and shear, which exhibits similar E_{ind} as the other two units (Fig. 3). On the other hand, all three units of the interior share a similar nanostructure of densely packed, highly aligned, yet crimped collagen fibrils (Fig. 6a,b). This leads to the similar E_{ind} when nanoindentation is performed normal to the fiber axis, regardless of the cross-section orientation or structural unit type. Therefore, at least in the tension bearing outer zone, the complexity of meniscus mechanical function appears to be primarily manifested through the organization of different structural units at the micro-to-macro scales, while all the units share similar intrinsic mechanical properties. The ~ 10 μm thick surface layer, however, is an exception. This layer is composed of much thinner, randomly oriented transverse fibrils (Figs. 6,7) with significantly lower E_{ind} than all other units.

4.3 Heterogeneity across anatomical zones

Between the tension-bearing outer and middle zones [3] and the compression-bearing inner zone [4], the circumferential fibers show marked variations in micromechanical properties (Fig. 4a). The lower E_{ind} of the inner zone suggests that the decrease in collagen fibril diameter, density and organization (Figs. 6,7) most likely outweighs the effect of increased compression-bearing proteoglycans in the inner zone [6, 7]. Meanwhile, the reduced degree of anisotropy in E_{ind} in the inner zone can also be attributed to both the decreased alignment of collagen fibers (lower κ, Fig. 7b) and the increase in “amorphous” proteoglycans that are more isotropic in their mechanical contributions.

In contrast to the circumferential fibers, all other structural units do not exhibit such zonal heterogeneity (Fig. 4b). These units do not directly contribute to the tension-compression load bearing functions of the meniscus. Instead, they mainly serve to maintain the integrity of circumferential fibers. Their micromechanical properties are therefore not directly impacted by the zonal variations in meniscus loading conditions. For the surface and the superficial layer, both the collagen orientation and E_{ind} are similar from inner to outer zones, suggesting similar functions across anatomical regions, possibly including surface load transmission, lubrication and stabilization of the circumferential fibers. For the radial tie fibers, the function of integrating circumferential fibers and sustaining shear stresses is likely less important in the inner zone. However, such changes are manifested through its arborization into smaller sheets and bundles, reduced diameter and alignment within the fiber (Fig. 7) and decreased density from outer to inner zones, instead of the modulus determined by the local fibril nanostructure (Fig. 6).

4.4 Heterogeneity of time-dependent micromechanics

In soft tissues, time-dependent mechanics can be attributed to both poroelasticity that is due to fluid-matrix interactions [54], and intrinsic viscoelasticity that is due to macromolecular friction amongst matrix macromolecules [55]. Given the substantial heterogeneity of the meniscus ECM, it is unlikely for different zones or different structural units to share the same molecular-level time-dependent mechanisms. For example, proteoglycans can be a major player in the hydraulic permeability and intrinsic viscoelasticity of the inner zone, while their contribution to the outer zone mechanics is less important. Therefore, in the presence of heterogeneity of E_{ind}, the relative homogeneity in E_∞/E_0, τ_1 and τ_2 (Fig. 5a,b) indicates an important mechanical design principle of the meniscus ECM: all the interior structural units, despite their compositional or structural differences, possess similar relative time-dependent mechanical characteristics. This feature can be an effective means to minimize the extent of the redistribution in local stresses and strains, and in the extent of stress concentration at the structural unit boundaries during time-dependent deformation. A similar feature is observed at larger scales, where microindentation ($R \approx 100$ μm) detected similar E_∞/E_0 across various anatomical sites of the meniscus surface [21] and the interior horizontal cross-sections [22]. Such self-consistency in time-dependent mechanics is also found for cartilage ECM, where despite variations in proteoglycan content, collagen fibril architecture, hydraulic permeability and modulus, a constant poroelastic time constant was detected throughout cartilage depth [56]. On the other hand, the moderate anisotropy of τ_2 measured on the circumferential fibers in the outer zone (Figs. 2b,5b) highlights that viscoelastic deformation of the collagen fibrils can be different for orientations normal versus parallel to the fiber axis. In contrast, in the inner zone, with less organized collagen fibers and higher “amorphous” proteoglycan content, both τ_1 and τ_2 become isotropic.

To gain further insights into time-dependent mechanisms of the meniscus, we performed scaling analysis [57] to estimate the characteristic poroelastic time constant, τ_p. For the meniscus ECM, the hydraulic permeability is ~ 10^{-15} $m^4/(N•s)$ [44], and our nanoindentation results suggest that the aggregate modulus H_A is ~ 0.1 MPa. Under current nanoindentation configuration, we estimate the fluid flow length, $L_p \sim R \times \arccos[(R - D)/R] \approx 3$ μm [57], and thus, $\tau_p \sim L_p^2/(H_A k)$=0.1 sec [58]. In this study, τ_1 is ~ 0.1 sec and

τ_2 is ~ 10 sec, it is likely that poroelasticity could be a major factor for the short term relaxation, while the long term relaxation is mostly governed by intrinsic viscoelasticity. This trend is consistent with the time-dependent mechanics of cartilage at the microscale: when L_p is ~ 1 μm, poroelastic deformation is much faster than viscoelasticity [57, 59]. However, this trend is reversed at the macroscale, when L_p is ~ 1 mm [60]. This is because τ_p scales parabolically with L_p [58], τ_p at μm-scale is several orders faster than that at mm-scale [57, 59], while the viscoelastic times remain consistent despite the variation of L_p [61]. Similarly, for hydrogels, a slower τ_p than viscoelastic times is also detected under macroscopic indentation [62]. For this study, however, we did not modulate L_p, and thus, we cannot accurately determine the contribution of poro- versus viscoelasticity. Ongoing studies are applying our custom AFM-nanorheometer [57, 59] to separate the two mechanisms in native meniscus by systemically varying L_p.

4.5 Implications for meniscus tissue function and repair

For meniscus repair, in order to restore the normal meniscus-cartilage contact and loading, it is critical to simulate the shape and bulk tissue-level properties of the meniscus [3, 4, 44, 55]. The direct deterministic benchmarks for successful regeneration are the mechanical properties of native meniscus at the macroscale, rather than at the nano- or microscale [63]. However, the specialized, complex tissue-level biomechanical functions of native meniscus are endowed by the highly complex features of its ECM at smaller lengths. In addition, recent studies suggested that the nanostructure and nanomechanical properties of the meniscus ECM are important factors that regulate cell migration [64] and mechanotransduction [11]. This work can thus provide insights for better mimicking the complex properties of native tissue, and for helping direct meniscus cell behavior in engineered scaffolds.

One limitation of this study is that all the tests were performed at zero tissue-level strain. Given the salient nonlinearity of the meniscus tissue biomechanics [44], the outcomes do not necessarily represent the micromechanical behaviors at higher tissue strains. Currently, studying such behavior is hindered by the technical challenge of applying tensile strain to AFM specimens in fluid. To this day, however, AFM imaging has been performed on thin films in tension [65]. This technique can be modified to enable micromechanical studies of the meniscus under tension and in fluid.

5. CONCLUSIONS

This study connected the anisotropy and heterogeneity in the elastic and time-dependent micromechanical properties of the meniscus ECM with its collagen fibril nanostructure. The anisotropy in modulus is due to differences in collagen fibril deformation modes with regard to its fiber axis. Heterogeneity is associated with the collagen fiber organization among different structural units, while these units share similar nanostructural and micromechanical properties. In contrast to the heterogeneity in modulus, the degree of elasticity and relaxation time constants are more homogeneous and isotropic. These results contribute to a basic understanding of multiscale structure-mechanics relationships of the meniscus ECM, which

has the potential to improve the regeneration of meniscus through modulating the local micromechanical environment.

Acknowledgments

This work was supported by the National Institutes of Health, Grants AR066824 to LH, EB002425 to RLM, and AR050950 to the Penn Center for Musculoskeletal Disorders (PCMD).

References

1. Makris EA, Hadidi P, Athanasiou KA. The knee meniscus: structure-function, pathophysiology, current repair techniques, and prospects for regeneration. Biomaterials. 2011; 32:7411–31. [PubMed: 21764438]
2. Petersen W, Tillmann B. Collagenous fibril texture of the human knee joint menisci. Anat Embryol. 1998; 197:317–24. [PubMed: 9565324]
3. Fithian DC, Kelly MA, Mow VC. Material properties and structure-function-relationships in the menisci. Clin Orthop Relat Res. 1990; 252:19–31.
4. Sweigart MA, Athanasiou KA. Tensile and compressive properties of the medial rabbit meniscus. Proc Inst Mech Eng [H]. 2005; 219:337–47.
5. Fukubayashi T, Kurosawa H. The contact area and pressure distribution pattern of the knee. A study of normal and osteoarthrotic knee joints. Acta Orthop Scand. 1980; 51:871–9. [PubMed: 6894212]
6. Sanchez-Adams J, Willard VP, Athanasiou KA. Regional variation in the mechanical role of knee meniscus glycosaminoglycans. J Appl Physiol. 2011; 111:1590–6. [PubMed: 21903884]
7. Vanderploeg EJ, Wilson CG, Imler SM, Ling CH, Levenston ME. Regional variations in the distribution and colocalization of extracellular matrix proteins in the juvenile bovine meniscus. J Anat. 2012; 221:174–86. [PubMed: 22703476]
8. Skaggs DL, Warden WH, Mow VC. Radial tie fibers influence the tensile properties of the bovine medial meniscus. J Orthop Res. 1994; 12:176–85. [PubMed: 8164089]
9. Andrews SH, Rattner JB, Abusara Z, Adesida A, Shrive NG, Ronsky JL. Tie-fibre structure and organization in the knee menisci. J Anat. 2014; 224:531–7. [PubMed: 24617800]
10. Rattner JB, Matyas JR, Barclay L, Holowaychuk S, Sciore P, Lo IK, Shrive NG, Frank CB, Achari Y, Hart DA. New understanding of the complex structure of knee menisci: implications for injury risk and repair potential for athletes. Scand J Med Sci Sports. 2011; 21:543–53. [PubMed: 20459477]
11. Han WM, Heo SJ, Driscoll TP, Delucca JF, McLeod CM, Smith LJ, Duncan RL, Mauck RL, Elliott DM. Microstructural heterogeneity directs micromechanics and mechanobiology in native and engineered fibrocartilage. Nat Mater. 2016; 15:477–84. [PubMed: 26726994]
12. Vanden Berg-Foels WS, Scipioni L, Huynh C, Wen X. Helium ion microscopy for high-resolution visualization of the articular cartilage collagen network. J Microsc. 2012; 246:168–76. [PubMed: 22416783]
13. Jones RS, Keene GC, Learmonth DJ, Bickerstaff D, Nawana NS, Costi JJ, Pearcy MJ. Direct measurement of hoop strains in the intact and torn human medial meniscus. Clin Biomech (Bristol, Avon). 1996; 11:295–300.
14. Badlani JT, Borrero C, Golla S, Harner CD, Irrgang JJ. The effects of meniscus injury on the development of knee osteoarthritis: data from the osteoarthritis initiative. Am J Sports Med. 2013; 41:1238–44. [PubMed: 23733830]
15. Lotz MK, Kraus VB. Posttraumatic osteoarthritis: pathogenesis and pharmacological treatment options. Arthritis Res Ther. 2010; 12:211. [PubMed: 20602810]
16. Mauck RL, Burdick JA. From repair to regeneration: biomaterials to reprogram the meniscus wound microenvironment. Ann Biomed Eng. 2015; 43:529–42. [PubMed: 25650096]
17. Rhee S, Puetzer JL, Mason BN, Reinhart-King CA, Bonassar LJ. 3D bioprinting of spatially heterogeneous collagen constructs for cartilage tissue engineering. ACS Biomater Sci Eng. 2016; 2:1800–5.

18. Fisher MB, Henning EA, Soegaard N, Bostrom M, Esterhai JL, Mauck RL. Engineering meniscus structure and function via multi-layered mesenchymal stem cell-seeded nanofibrous scaffolds. J Biomech. 2015; 48:1412–9. [PubMed: 25817333]
19. Han WM, Heo S-J, Driscoll TP, Smith LJ, Mauck RL, Elliott DM. Macro- to microscale strain transfer in fibrous tissues is heterogeneous and tissue-specific. Biophys J. 2013; 105:807–17. [PubMed: 23931328]
20. Mow, VC., Gu, WY., Chen, FH. Structure and function of articular cartilage and meniscus. In: Mow, VC., Huskes, R., editors. Basic Orthopaedic Biomechanics and Mechanobiology. 3rd. Philadephia: Lippincott, Williams & Wilkins; 2003. p. 181-258.
21. Moyer JT, Abraham AC, Donahue TLH. Nanoindentation of human meniscal surfaces. J Biomech. 2012; 45:2230–5. [PubMed: 22789734]
22. Moyer JT, Priest R, Bouman T, Abraham AC, Donahue TLH. Indentation properties and glycosaminoglycan content of human menisci in the deep zone. Acta Biomater. 2013; 9:6624–9. [PubMed: 23321302]
23. Sanchez-Adams J, Wilusz RE, Guilak F. Atomic force microscopy reveals regional variations in the micromechanical properties of the pericellular and extracellular matrices of the meniscus. J Orthop Res. 2013; 31:1218–25. [PubMed: 23568545]
24. Kwok J, Grogan S, Meckes B, Arce F, Lal R, D'Lima D. Atomic force microscopy reveals age-dependent changes in nanomechanical properties of the extracellular matrix of native human menisci: implications for joint degeneration and osteoarthritis. Nanomed Nanotech Biol Med. 2014; 10:1777–85.
25. Li Q, Doyran B, Gamer LW, Lu XL, Qin L, Ortiz C, Grodzinsky AJ, Rosen V, Han L. Biomechanical properties of murine meniscus surface via AFM-based nanoindentation. J Biomech. 2015; 48:1364–70. [PubMed: 25817332]
26. McNulty AL, Guilak F. Mechanobiology of the meniscus. J Biomech. 2015; 48:1469–78. [PubMed: 25731738]
27. Cucchiarini M, McNulty AL, Mauck RL, Setton LA, Guilak F, Madry H. Advances in combining gene therapy with cell and tissue engineering-based approaches to enhance healing of the meniscus. Osteoarthr Cartilage. 2016; 24:1330–9.
28. Rongen JJ, van Tienen TG, van Bochove B, Grijpma DW, Buma P. Biomaterials in search of a meniscus substitute. Biomaterials. 2014; 35:3527–40. [PubMed: 24477194]
29. Ionescu LC, Lee GC, Garcia GH, Zachry TL, Shah RP, Sennett BJ, Mauck RL. Maturation state-dependent alterations in meniscus integration: Implications for scaffold design and tissue engineering. Tissue Eng A. 2011; 17:193–204.
30. Hutter JL, Bechhoefer J. Calibration of atomic-force microscope tips. Rev Sci Instrum. 1993; 64:1868–73.
31. Dimitriadis EK, Horkay F, Maresca J, Kachar B, Chadwick RS. Determination of elastic moduli of thin layers of soft material using the atomic force microscope. Biophys J. 2002; 82:2798–810. [PubMed: 11964265]
32. Sweigart MA, Zhu CF, Burt DM, deHoll PD, Agrawal CM, Clanton TO, Athanasiou KA. Intraspecies and interspecies comparison of the compressive properties of the medial meniscus. Ann Biomed Eng. 2004; 32:1569–79. [PubMed: 15636116]
33. Mattice JM, Lau AG, Oyen ML, Kent RW. Spherical indentation load-relaxation of soft biological tissues. J Mater Res. 2006; 21:2003–10.
34. Oyen ML. Spherical indentation creep following ramp loading. J Mater Res. 2005; 20:2094–100.
35. Lau A, Oyen ML, Kent RW, Murakami D, Torigaki T. Indentation stiffness of aging human costal cartilage. Acta Biomater. 2008; 4:97–103. [PubMed: 17702680]
36. Hauch KN, Oyen ML, Odegard GM, Donahue TLH. Nanoindentation of the insertional zones of human meniscal attachments into underlying bone. J Mech Behav Biomed Mater. 2009; 2:339–47. [PubMed: 19627840]
37. Bush BG, Shapiro JM, DelRio FW, Cook RF, Oyen ML. Mechanical measurements of heterogeneity and length scale effects in PEG-based hydrogels. Soft Matter. 2015; 11:7191–200. [PubMed: 26255839]

38. Bray DF, Bagu J, Koegler P. Comparison of hexamethyldisilazane (HMDS), peldri II, and critical-point drying methods for scanning electron-microscopy of biological specimens. Microsc Res Tech. 1993; 26:489–95. [PubMed: 8305726]
39. Krumbein WC. Preferred orientation of pebbles in sedimentary deposits. J Geol. 1939; 47:673–706.
40. Mardia, KV., Jupp, PE. Directional Statistics. London, UK: John Wiley & Sons, Ltd; 2000. Tests of von Mises distributions; p. 119-43.
41. Abraham AC, Edwards CR, Odegard GM, Donahue TL. Regional and fiber orientation dependent shear properties and anisotropy of bovine meniscus. J Mech Behav Biomed Mater. 2011; 4:2024–30. [PubMed: 22098902]
42. Wang H, Abhilash AS, Chen CS, Wells RG, Shenoy VB. Long-range force transmission in fibrous matrices enabled by tension-driven alignment of fibers. Biophys J. 2014; 107:2592–603. [PubMed: 25468338]
43. Wang L, Ortiz C, Boyce MC. Mechanics of indentation into micro- and nanoscale forests of tubes, rods, or pillars. J Eng Mater Technol. 2011; 133:011014.
44. Proctor CS, Schmidt MB, Whipple RR, Kelly MA, Mow VC. Material properties of the normal medial bovine meniscus. J Orthop Res. 1989; 7:771–82. [PubMed: 2677284]
45. Danso EK, Honkanen JT, Saarakkala S, Korhonen RK. Comparison of nonlinear mechanical properties of bovine articular cartilage and meniscus. J Biomech. 2014; 47:200–6. [PubMed: 24182695]
46. Lanir Y. Constitutive equations for fibrous connective tissues. J Biomech. 1983; 16:1–12. [PubMed: 6833305]
47. Szczesny SE, Peloquin JM, Cortes DH, Kadlowec JA, Soslowsky LJ, Elliott DM. Biaxial tensile testing and constitutive modeling of human supraspinatus tendon. J Biomech Eng. 2012; 134:021004. [PubMed: 22482671]
48. Han L, Wang L, Chia K-K, Cohen RE, Rubner MF, Boyce MC, Ortiz C. Geometrically controlled mechanically responsive polyelectrolyte tube arrays. Adv Mater. 2011; 23:4667–73. [PubMed: 21919084]
49. Vlassak JJ, Nix WD. Measuring the elastic properties of anisotropic materials by means of indentation experiments. J Mech Phys Solids. 1994; 42:1223–45.
50. Swadener JG, Rho J-Y, Pharr GM. Effects of anisotropy on elastic moduli measured by nanoindentation in human tibial cortical bone. J Biomed Mater Res A. 2001; 57:108–12.
51. Wang L, Song J, Ortiz C, Boyce MC. Anisotropic design of a multilayered biological exoskeleton. J Mater Res. 2009; 24:3477–94.
52. Han L, Wang L, Song J, Boyce MC, Ortiz C. Direct quantification of the mechanical anisotropy and fracture of an individual exoskeleton layer via uniaxial compression of micropillars. Nano Lett. 2011; 11:3868–74. [PubMed: 21755939]
53. Fan Z, Swadener JG, Rho JY, Roy ME, Pharr GM. Anisotropic properties of human tibial cortical bone as measured by nanoindentation. J Orthop Res. 2002; 20:806–10. [PubMed: 12168671]
54. Spilker RL, Donzelli PS, Mow VC. A transversely isotropic biphasic finite element model of the meniscus. J Biomech. 1992; 25:1027–45. [PubMed: 1517263]
55. Zhu W, Chern KY, Mow VC. Anisotropic viscoelastic shear properties of bovine meniscus. Clin Orthop Relat Res. 1994:34–45. [PubMed: 8070209]
56. Nia HT, Li Y, Wang Y, Soltani I, Chubinskaya S, Youcef-Toumi K, Ortiz C, Grodzinsky AJ. Depth-dependent self-stiffening, energy dissipation and poroelastic properties of normal human cartilage via broad-spectrum dynamic nanoindentation. Trans Orthop Res Soc. 2013; 59:309.
57. Han L, Frank EH, Greene JJ, Lee H-Y, Hung H-HK, Grodzinsky AJ, Ortiz C. Time-dependent nanomechanics of cartilage. Biophys J. 2011; 100:1846–54. [PubMed: 21463599]
58. Mow VC, Kuei SC, Lai WM, Armstrong CG. Biphasic creep and stress relaxation of articular cartilage in compression: theory and experiments. J Biomech Eng. 1980; 102:73–84. [PubMed: 7382457]
59. Nia HT, Bozchalooi IS, Li Y, Han L, Hung HH, Frank E, Youcef-Toumi K, Ortiz C, Grodzinsky A. High-bandwidth AFM-based rheology reveals that cartilage is most sensitive to high loading rates at early stages of impairment. Biophys J. 2013; 104:1529–37. [PubMed: 23561529]

60. Kim Y-J, Bonassar LJ, Grodzinsky AJ. The role of cartilage streaming potential, fluid flow and pressure in the stimulation of chondrocyte biosynthesis during dynamic compression. J Biomech. 1995; 28:1055–66. [PubMed: 7559675]

61. June RK, Ly S, Fyhrie DP. Cartilage stress-relaxation proceeds slower at higher compressive strains. Arch Biochem Biophys. 2009; 483:75–80. [PubMed: 19111671]

62. Hu Y, Zhao X, Vlassak JJ, Suo Z. Using indentation to characterize the poroelasticity of gels. Appl Phys Lett. 2010; 96:121904.

63. Setton LA, Guilak F, Hsu EW, Vail TP. Biomechanical factors in tissue engineered meniscal repair. Clin Orthop Relat Res. 1999:S254–72. [PubMed: 10546651]

64. Qu F, Pintauro MP, Haughan JE, Henning EA, Esterhai JL, Schaer TP, Mauck RL, Fisher MB. Repair of dense connective tissues via biomaterial-mediated matrix reprogramming of the wound interface. Biomaterials. 2015; 39:85–94. [PubMed: 25477175]

65. Yarysheva AY, Rukhlya EG, Yarysheva LM, Bagrov DV, Volynskii AL, Bakeev NF. The structural evolution of high-density polyethylene during crazing in liquid medium. Eur Polym J. 2015; 66:458–69.

Statement of Significance

Meniscal damage is a common cause of joint injury, which can lead to the development of posttraumatic osteoarthritis among young adults. Restoration of meniscus function requires repairing its highly heterogeneous and complex extracellular matrix. Employing atomic force microscopy, this study quantifies the anisotropic and heterogeneous features of the meniscus extracellular matrix structure and mechanics. The meniscus micromechanical characteristics are connected with the collagen fibril nanostructure, and its variation with tissue anatomical locations. These results provide a fundamental structure-mechanics knowledge benchmark, against which, repair and regeneration strategies can be developed and evaluated with respect to the specialized structural and functional complexity of the native tissue.

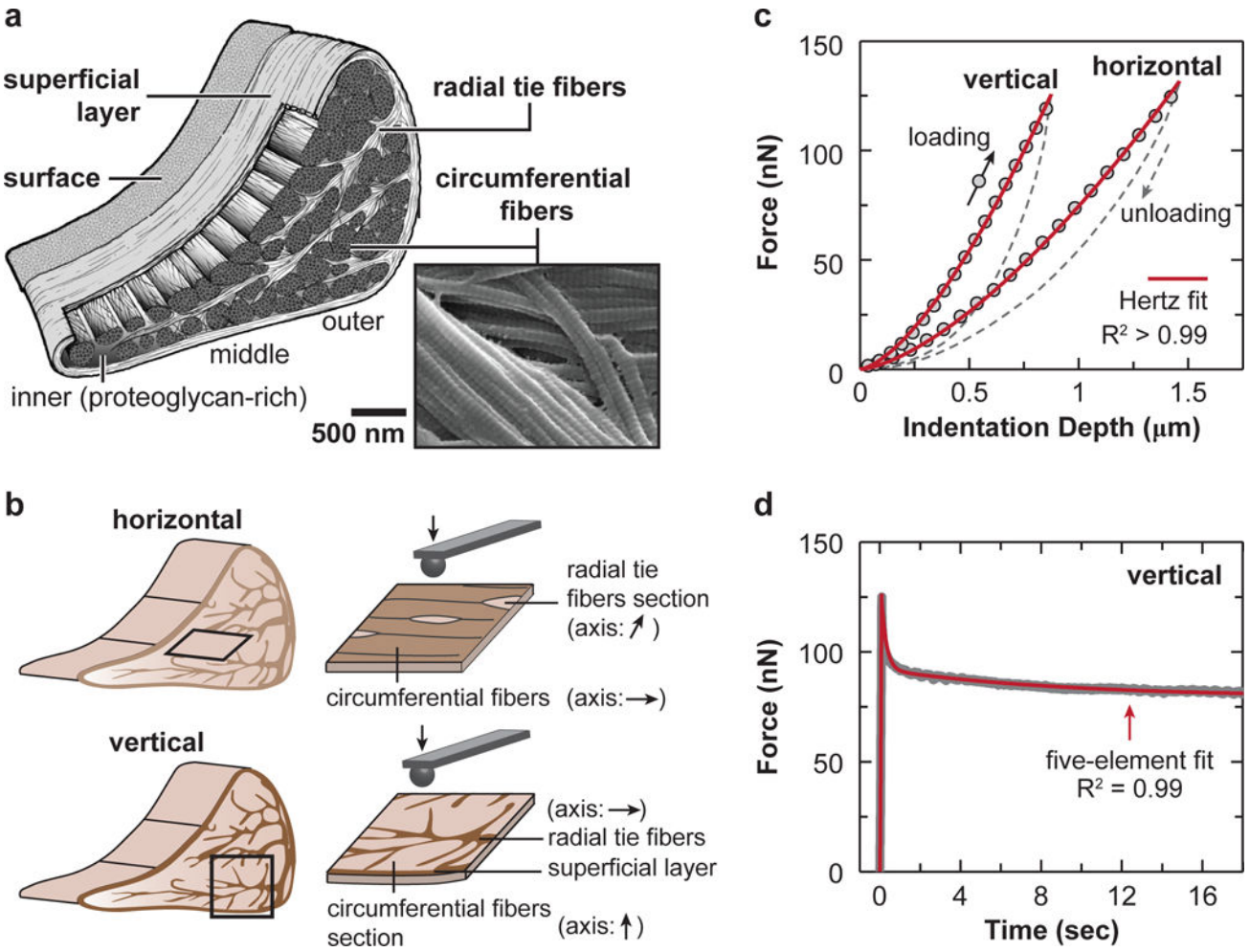

Fig. 1.

AFM-nanomechanical test set-up. (a) Schematic of the meniscus extracellular matrix (ECM) highlighting the four major structural units: surface, superficial layer, radial tie fibers and circumferential fibers, as well as the zonal variation. Scanning electron microscopy (SEM) image showing that two adjacent circumferential fibers are interconnected by fibrils spanning across them (white arrowhead). (b) Schematics of AFM-nanoindentation test on the horizontal and vertical sections, where the fiber axis orientation within each interior structural unit is shown. (c) Representative indentation force versus depth (*F-D*) curves measured on both horizontal and vertical sections of outer zone circumferential fibers, and corresponding Hertz model fit (tip radius $R \approx 5$ μm, spring constant $k \approx 0.6$ N/m, $R^2 > 0.99$). (d) Representative relaxation curve of temporal force, $F(t)$, versus time, measured on the vertical section of outer zone circumferential fibers, and corresponding five-element model fit ($R^2 = 0.99$).

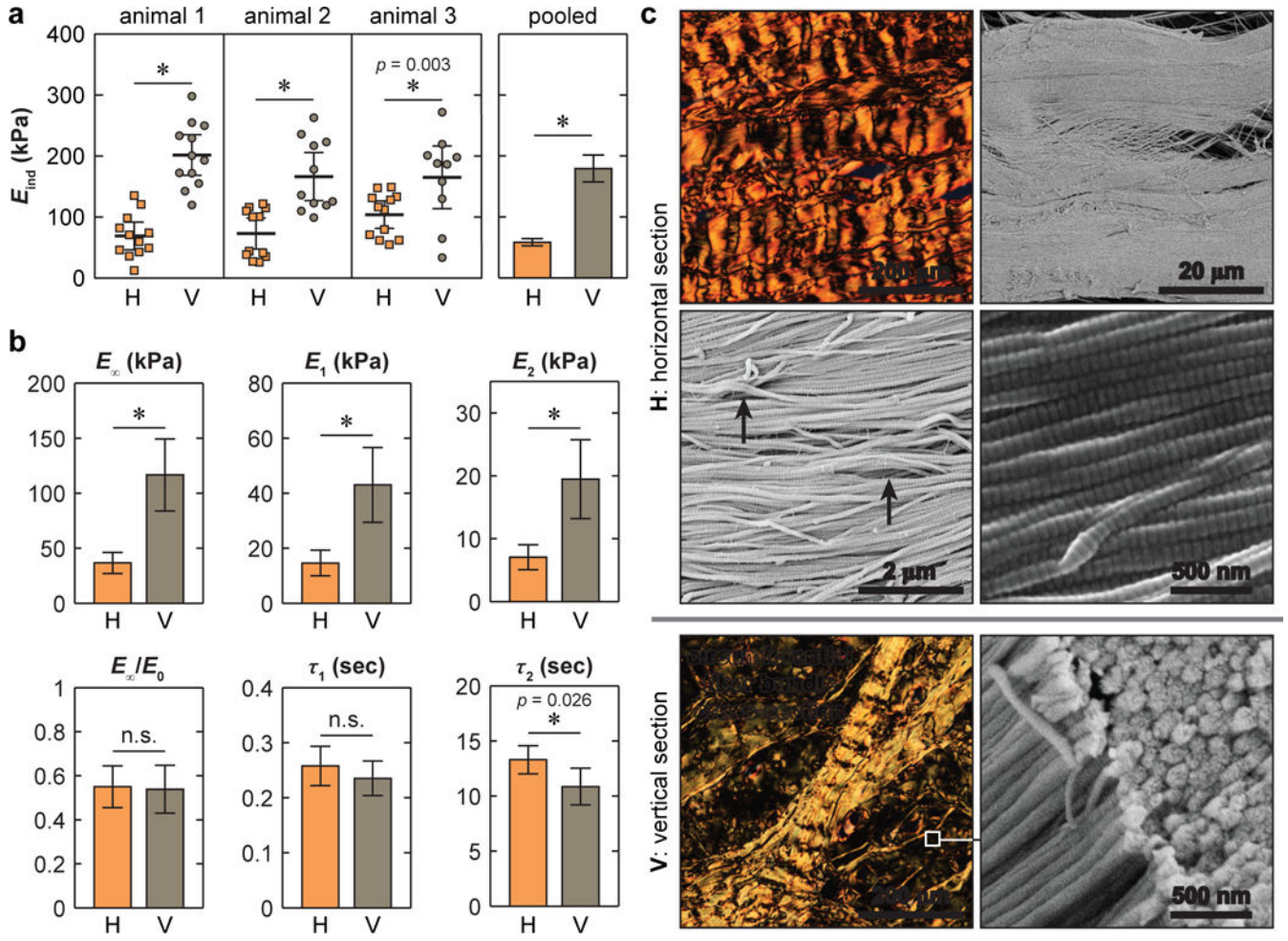

Fig. 2.

Micromechanical anisotropy of the circumferential fibers. (a) Comparison of effective indentation modulus, E_{ind}, measured on horizontal versus vertical sections, where comparison of individual locations within each animal and pooled results yield the same significant results (*: $p < 0.01$ via Mann-Whitney U test, and $p < 0.001$ if not provided). (b) Comparison of time-dependent micromechanical properties between horizontal and vertical sections: equilibrium modulus (E_∞), degree of elasticity (E_∞/E_0), time coefficients and moduli for short term (E_1, τ_1) and long term (E_2, τ_2) relaxations (mean ± 95% CI of ≥ 20 locations pooled from $n = 3$ animals, *: $p < 0.05$ via Mann-Whitney U test, and $p < 0.001$ if not provided. H: horizontal section, V: vertical section). (c) Polarized light microscopy images of Alcian Blue/Picrosirius Red stained sections showing collagen fiber microstructure, and SEM images showing collagen fibril nanostructure in the deeper zone (white arrowheads: fiber-level crimping with periodicity ~ 30 μm, black arrows: fibril-level crimping with periodicity ~ 1 μm).

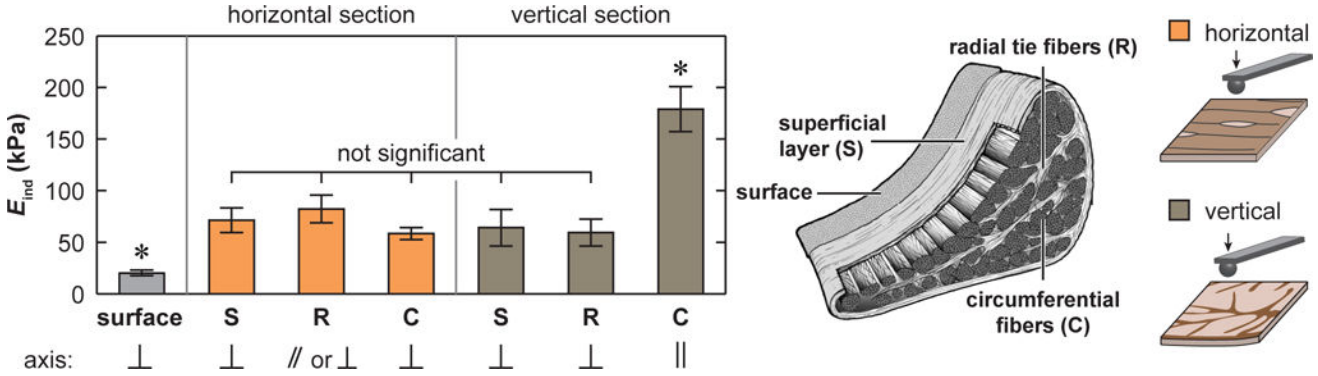

Fig. 3.

Heterogeneity of the effective indentation modulus, E_{ind}, across different meniscus ECM structural units of the outer zone (mean ± 95% CI of ≥ 20 locations pooled from $n = 3$ animals, *: $p < 0.0001$ from Kruskal-Wallis test followed by Tukey-Kramer multiple comparison).

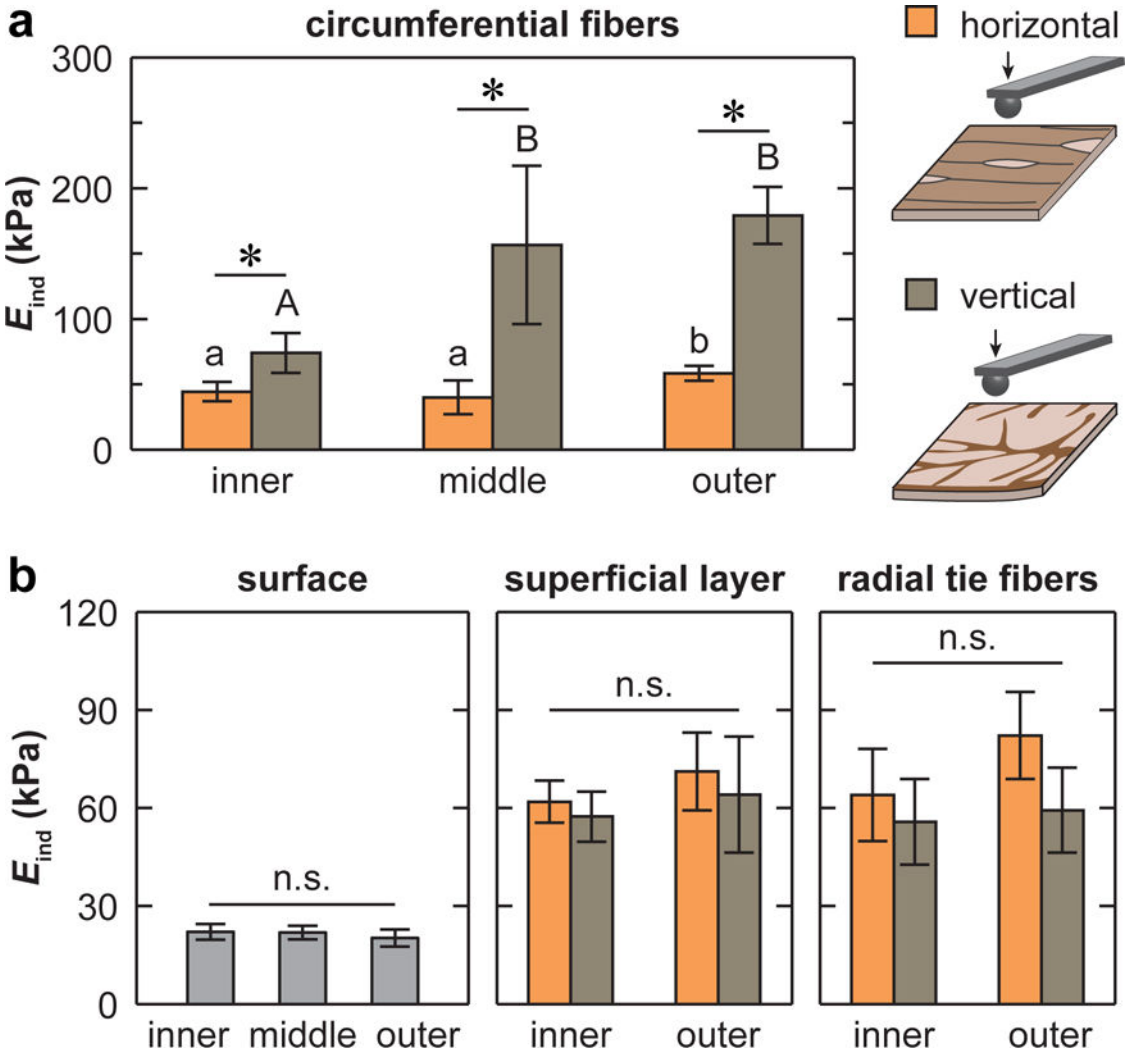

Fig. 4.

Heterogeneity of the effective indentation modulus, E_{ind}, across the inner, middle and outer zones of the meniscus ECM. (a) E_{ind} of circumferential fibers, for each cross-section type, different letters indicate significant difference in E_{ind} across zones via Kruskal-Wallis test followed by Tukey-Kramer multiple comparison, (*: $p < 0.01$ between horizontal and vertical sections within each zone via MannWhitney U test). (b) E_{ind} of other structural units, where no significance was found across zones or between cross-sections (mean ± 95% CI of ≥ 20 locations for each structural unit, pooled from $n = 3$ animals).

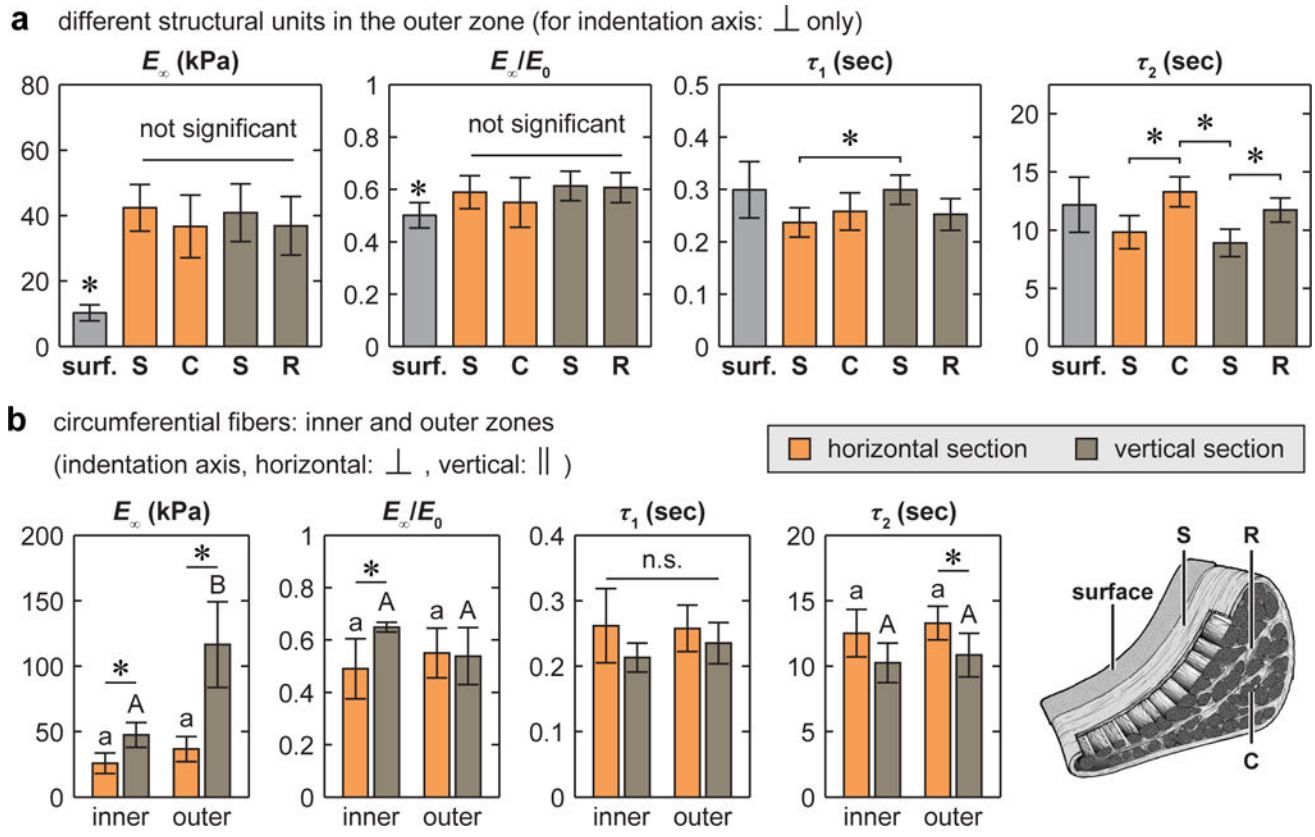

Fig. 5.

Heterogeneity of time-dependent micromechanical properties of the meniscus ECM: equilibrium modulus, E_∞, degree of elasticity, E_∞/E_0, time constants for short term (τ_1) and long term (τ_2) relaxations (E_1 and E_2 followed the same trend as E_∞, therefore are not shown, where $E_1 > E_2$). (a) Comparison across different structural units of the outer zone on horizontal and vertical sections, in which the indentation was performed normal to their fiber axes (*: $p < 0.05$ from Kruskal-Wallis test followed by Tukey-Kramer multiple comparison). (b) Comparison between the inner versus outer zones of the circumferential fibers on horizontal and vertical sections (for each cross-section type, different letters indicate significant difference between inner versus outer zone via Kruskal-Wallis test followed by Tukey-Kramer multiple comparison, *: $p < 0.05$ between horizontal and vertical sections within each zone via Mann-Whitney U test, all data are shown as mean ± 95% CI of ≥ 20 locations pooled from $n = 3$ animals).

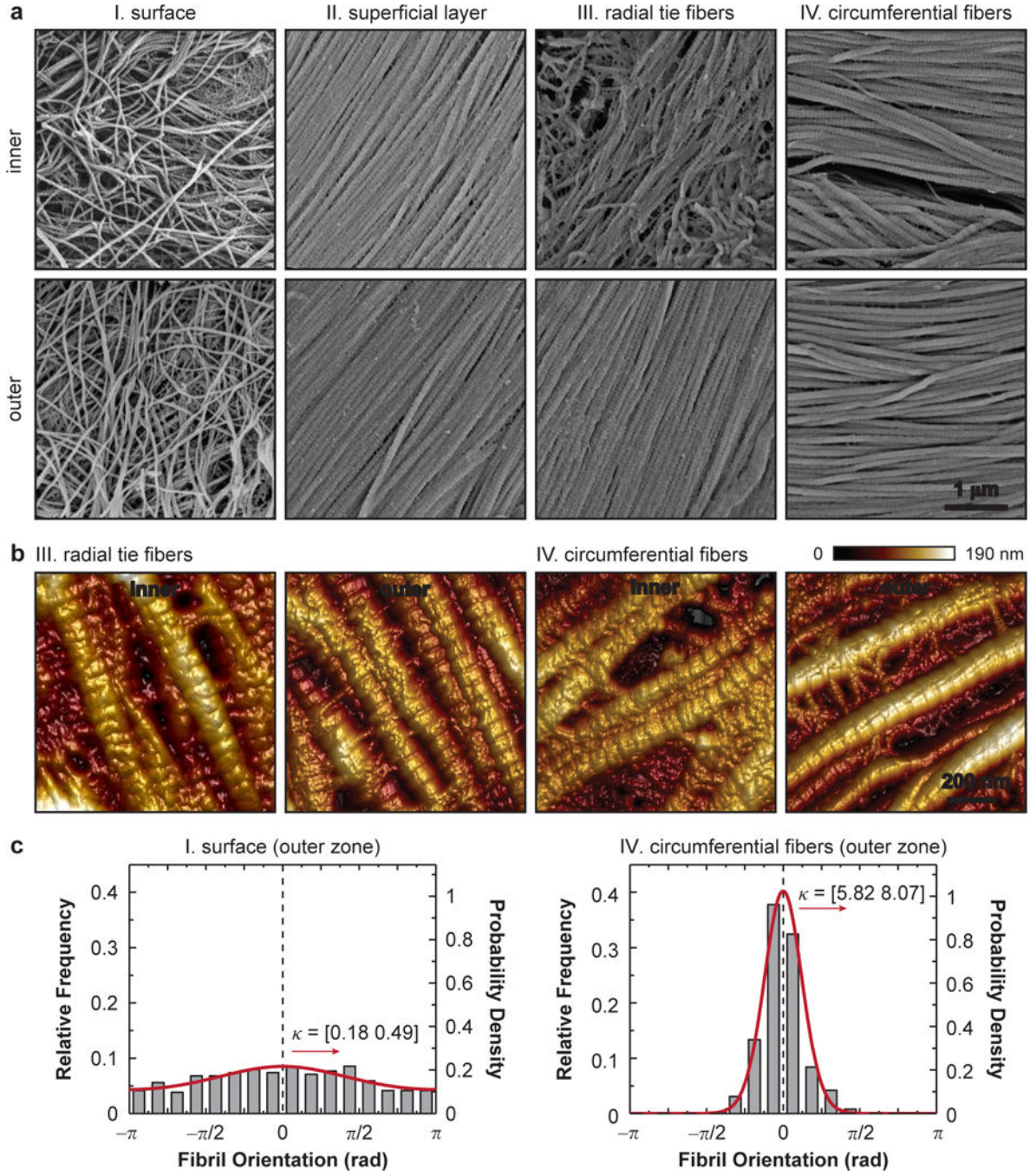

Fig. 6.

Nanostructure of collagen fibrils in the meniscus ECM. (a) Scanning electron microscopy (SEM) images of each structural unit show the dimension and alignment of collagen fibrils. (b) Higher resolution tapping mode AFM images show the presence of proteoglycans between fibrils. (c) Relative frequency of collagen fibril orientation distribution and corresponding von Mises fit of the intact surface and circumferential fibers in the outer zone. Data are pooled from $n = 3$ animals for each unit and shown with the 95% CI of κ, the von Mises concentration. The y-axes of the frequency probability mass function (left) and the

von Mises probability density function fit (right) are adjusted to account for the interval of each frequency bin, which is $\pi/8$.

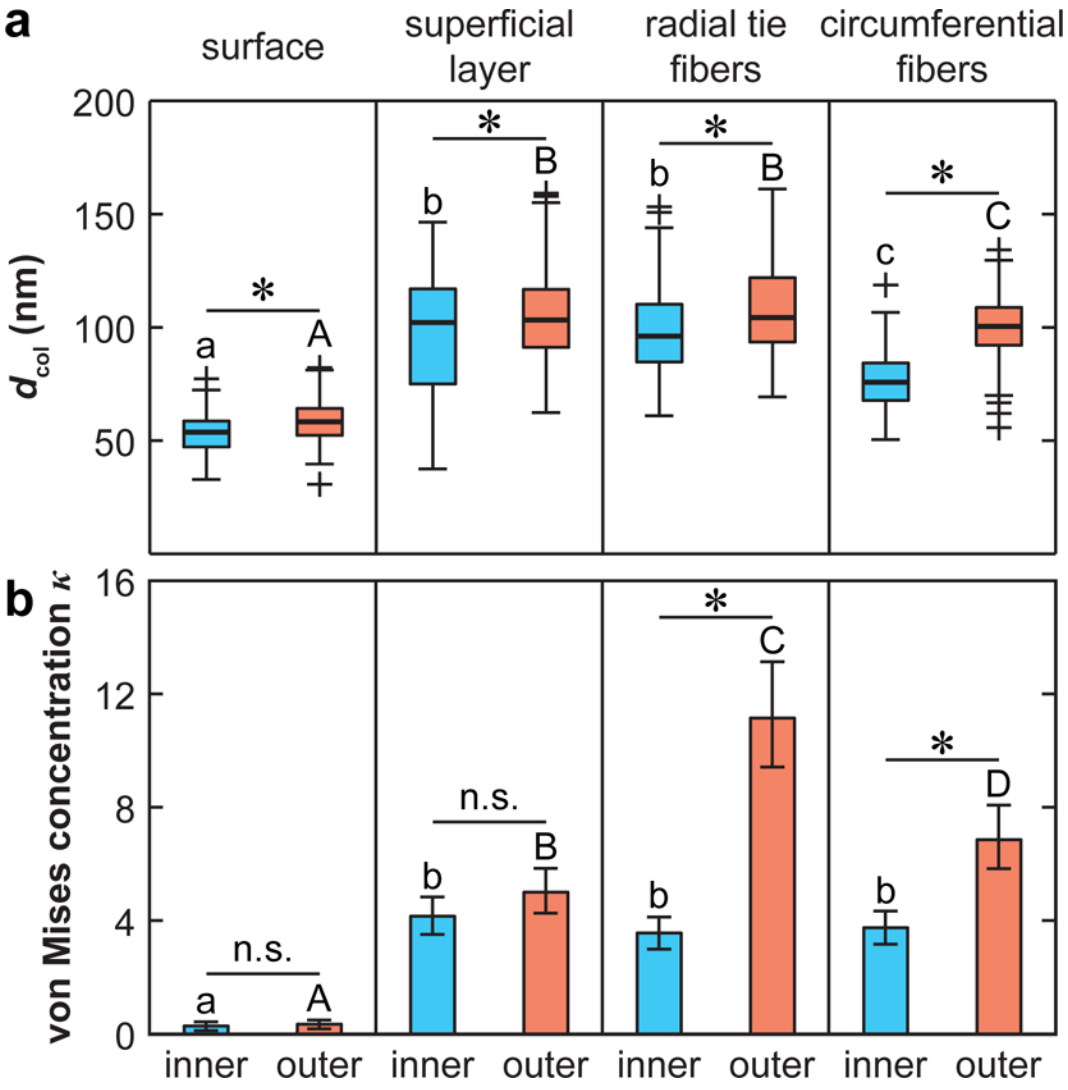

Fig. 7.

Summary of collagen fibril nanostructure in meniscus ECM inner and outer zones. (a) Box-and-whisker plot of diameter, d_{col}, distribution (≥ 300 fibrils pooled from $n = 3$ animals for each unit. Different letters indicate significant difference in d_{col} across different units within the same zone, and *: $p < 0.0001$ between inner versus outer zone for the same structural unit via one-way ANOVA followed by Tukey-Kramer multiple comparison). (b) von Mises concentration parameter, κ (mean ± 95% CI, estimated from > 300 fibrils pooled from $n = 3$ animals for each unit. Different letters indicate significant difference in κ across different units within the same zone, and *: $p < 0.01$ between inner versus outer zone for the same structural unit via Mardia and Jupp test of equal concentration followed by Bonferroni correction).

Table 1

Summary of the relationships between indentation orientation and the collagen fiber axis for each structural unit on the horizontal and vertical cross-sections.

structural units	cross-section type	
	horizontal	vertical
I. surface	normal (⊥)	–
II. superficial layer	normal (⊥)	normal (⊥)
III. radial tie fibers	oblique (//) or normal (⊥)	normal (⊥)
IV. circumferential fibers	normal (⊥)	parallel (∥)